

See discussions, stats, and author profiles for this publication at: <https://www.researchgate.net/publication/51859945>

Assembly Behavior of Iron Oxide-Capped Janus Particles in a Magnetic Field

ARTICLE *in* LANGMUIR · DECEMBER 2011

Impact Factor: 4.46 · DOI: 10.1021/la203969f · Source: PubMed

CITATIONS

30

READS

61

4 AUTHORS:



Bin Ren

CUNY Graduate Center

4 PUBLICATIONS 44 CITATIONS

[SEE PROFILE](#)



Aleksey Ruditskiy

Georgia Institute of Technology

11 PUBLICATIONS 205 CITATIONS

[SEE PROFILE](#)



Kevin Song

City College of New York

7 PUBLICATIONS 116 CITATIONS

[SEE PROFILE](#)



Ilona Kretzschmar

City College of New York

93 PUBLICATIONS 2,206 CITATIONS

[SEE PROFILE](#)

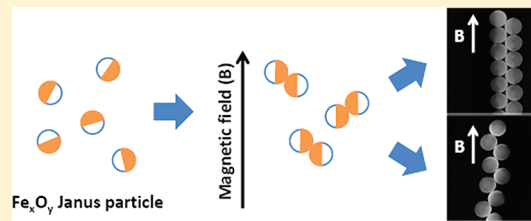
Assembly Behavior of Iron Oxide-Capped Janus Particles in a Magnetic Field

Bin Ren, Aleksey Ruditskiy, Jung Hun (Kevin) Song, and Ilona Kretzschmar*

Department of Chemical Engineering, City College of New York, City University of New York, 140th St. and Convent Ave., New York, New York 10031, United States

 Supporting Information

ABSTRACT: Three types of iron oxide Janus particles are obtained by varying the deposition rate of iron in a 3:1 Ar/O₂ atmosphere during physical vapor deposition. Each type of iron oxide Janus particle shows a distinct assembly behavior when an external magnetic field is applied, i.e., formation of staggered chains, double chains, or no assembly. A detailed deposition rate diagram is obtained to identify the relationship between deposition rate and assembly behavior. The extent of iron oxidation is identified as the key parameter in determining the assembly behavior. In addition, the effects of particle volume fraction, thickness of the iron oxide cap, and assembly time on the final assembly behavior are studied. Cap thickness is shown not to influence the assembly behavior, while particle volume fraction and assembly time affect the chain growth rate and the chain length, but not the overall assembly behavior. The samples are characterized by optical, scanning electron, and atomic force microscopies.



1. INTRODUCTION

Recent studies of magnetic Janus particles have focused on the assembly behavior of the following three types of particles:¹ (i) particles with one magnetic hemisphere,^{2–5} (ii) fluorescently labeled magnetic particles with a nonmagnetic cap,^{6,7} and (iii) Janus particles with a magnetic cap.⁸ These magnetic Janus particles are of interest for use in applications due to their addressability by external fields. For example, superparamagnetic hydrogel Janus particles with one magnetic hemisphere have been proposed as ideal candidates for building of three-dimensional hydrogel superstructures with chemically and magnetically tunable complexity for tissue engineering and sensing applications.³ Magnetically modulated optical nanoprobes (MagMOONs) are fluorescently labeled magnetic particles coated with a nonmagnetic metal cap that emit a fluorescence signal. These MagMOONs can be used to measure chemical concentrations and probe local rheological properties⁷ by “blinking” in response to rotating magnetic fields. The functionalization of MagMOONs has resulted in new optical,⁹ magnetic,⁷ chemical,^{10–12} and electrical properties.^{10,13} More general, ferromagnetic micro- and nanoparticles have found application in display technology^{14,15} and biosensing⁴ and as ferro-¹⁶ and magnetorheological fluids.¹⁷ Linear and nonlinear rotations of driven magnetic micro-particles may lead to a new class of physiochemical micro- and nanoparticle sensors that may be of significant biomedical and technological importance.¹⁸

Particles with one magnetic hemisphere are typically fabricated by oil-in-water emulsion,² microfluidic,³ droplet templating,¹⁹ and spin-coating methods.⁵ Fluorescently labeled magnetic particles with a nonmagnetic cap and Janus particles with a magnetic cap have been fabricated by vapor

deposition^{10,13} or metal sputtering.^{20,21} These Janus particles can be assembled into various structures under an external electric^{1,3,8,22–25} or magnetic field.^{2,3,8} Assembly structures reported for magnetic Janus particles have been staggered chains,² chainlike or meshlike superstructures,³ and double and staggered chains.⁸ More specifically, Smoukov et al.⁸ reported the formation of staggered and double chains for Janus particles with 34 and 8 nm iron caps, respectively.

Iron and its oxides are interesting materials because they possess magnetic and electric properties that are closely related to their degree of oxidation. This characteristic makes them viable for applications such as magnetic storage media and spin transport devices,²⁶ band gap engineering,²⁷ magneto-rheological fluids,²⁸ and tunneling magneto-resistance devices.²⁹ Iron metal is a soft ferromagnetic material, γ -Fe₂O₃ and Fe₃O₄ are ferrimagnetic, and α -Fe₂O₃ and stoichiometric FeO are antiferromagnetic materials.³⁰ Of these oxides, stoichiometric FeO is not stable at room temperature decomposing into Fe₃O₄ and Fe below 570 °C.³¹ However, stable nonstoichiometric Fe_{1-x}O has been reported.^{27,32–34} Several studies have been performed with the goal of depositing iron oxides with a controlled Fe:O stoichiometric ratio using reactive sputtering in the presence of a 3:1 Ar/O₂ mixture,^{30,32–36} reactive laser deposition in the presence of oxygen,²⁷ and gas-phase deposition.³⁷

Here, we report the use of physical vapor deposition (PVD) to deposit a thin iron oxide film onto a monolayer of polystyrene particles in order to fabricate Janus particles with a

Received: October 11, 2011

Revised: December 9, 2011

Published: December 12, 2011



magnetizable iron oxide cap of controlled stoichiometric composition. Three distinct assembly behaviors are observed after exposure to a magnetic field. Figure 1 depicts schematic-

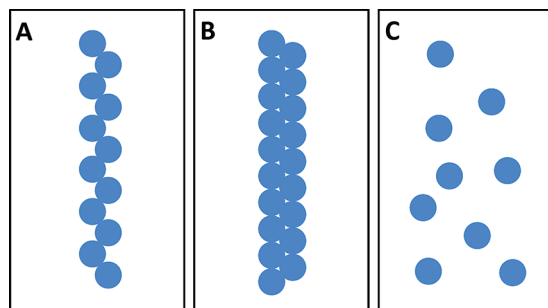


Figure 1. Schematic drawing of assembly structures observed for Janus particles with magnetic iron oxide caps: (A) staggered chain structure, (B) double chain structure, and (C) no assembly.

cally the three distinct assembly behaviors observed: (A) staggered chain, (B) double chain, and (C) no assembly. The assembly behavior exhibited by the Janus particles is found to depend strongly on the average deposition rate during the evaporation process.

2. EXPERIMENTAL SECTION

2.1. Materials. 2.4 μm sulfate-terminated polystyrene (sPS) spheres are purchased from Invitrogen Inc. as 8 wt % dispersed in water. The as-bought sPS sphere solution is concentrated to 16 wt % for monolayer assembly. To concentrate the particle solution, 500 μL of 8 wt % sPS particle solution is transferred into a centrifuge tube and spun for 5 min at 6000 rpm. Subsequently, 250 μL of the supernatant is removed, and a 16 wt % sPS particle solution is obtained after redispersion of particles by sonication. Microscope glass slides for monolayer assembly are obtained from Fisher Scientific, Inc., and cleaned using a 98% sulfuric acid (Acros) and Nochromix (Godax Laboratories, Inc.) mixture. 1/8 in. \times 1/8 in. iron (Fe) evaporation pellets (99.95%), which are used as the iron source during deposition, are purchased from Kurt J. Lesker Co. Three-strand tungsten wire baskets are used for evaporation (Ted Pella, Inc.). A custom blend of a 3:1 Ar/O₂ mixture from Airgas Inc. is used. Silicone wells with 9 mm diameter and 0.5 mm depth used for magnetic field assembly are purchased from Invitrogen.

2.2. Equipment. An sPS monolayer is fabricated using an NE-1000 programmable syringe pump from New Era Pump Systems, Inc. The iron oxide caps are generated by evaporation of iron in a benchtop metal evaporator system (Cressington 308 R, Ted Pella, Inc.) with a 3:1 Ar/O₂ atmosphere. The cap thickness is monitored with a quartz crystal microbalance inside the evaporator using a density setting of $\rho(\text{Fe}_2\text{O}_3) = 5.24 \text{ g/cm}^3$.³⁸ The deposition rate is adjusted via the filament current. The average deposition rate is determined using a Canon PowerShot SD870 IS digital camera recording the crystal balance reading as a function of time. Subsequent analysis of the video results in deposition thickness versus time plots. An optical microscope (Olympus BX51) equipped with a UI-2240-C camera (Imaging Development Systems GmbH) is used to monitor the assembly of the structures under magnetic field. A scanning electron microscope (EVO40 Zeiss) in high-resolution mode is used to image particle structures after magnetic field exposure. The strength of the constant magnetic field, generated by the U-shaped permanent magnet, is measured to be 0.08 T using a gaussmeter (Walker Scientific Inc. MG-3D). For the study of the influence of cap thickness, a NanoScope IIIa atomic force microscope (AFM) from Digital Instruments is used to characterize the thickness of the iron oxide deposits left behind on the glass slides after particle removal. All samples are scanned using tapping mode with a scan rate of 2 Hz and a scan area of 12 \times 12 μm . The AFM tip is a nonmagnetic silicon probe

from NanoProbe, with a tip length of 125 μm and a tapping frequency ranging from 307 to 374 kHz. The thickness of the film is measured in three spots on each sample, and values are reported with one standard deviation.

2.3. Janus Particle Fabrication and Assembly. Figure 2 shows a schematic representation of the Janus particle preparation and

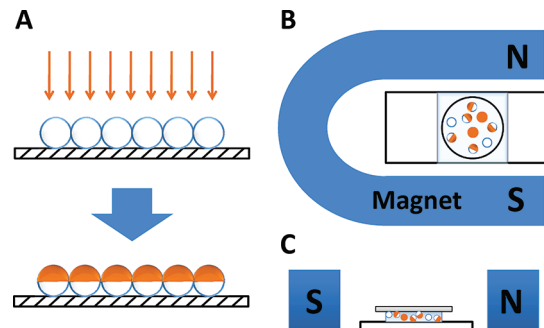


Figure 2. Schematic drawing of Janus particle fabrication and magnetic field assembly setup. (A) Janus particle fabrication. (B) Top and (C) side view of magnetic field assembly setup. Key: O, polystyrene; \ominus , Fe_xO_y, Janus particle; \square , silicon dioxide.

assembly process. A loosely packed (~50% coverage) monolayer of 2.4 μm sPS particles is fabricated by dragging 9 μL of a 16 wt % sPS particle solution over a pretreated hydrophilic glass slide using a convective deposition method adapted from Prevo et al.³⁹ A dragging rate of 5 mL/min is used and is adjusted, if needed, in order to account for variations in the ambient humidity and temperature. Three glass slides with loosely packed monolayers are placed on the stage underneath the tungsten filament in the evaporator at a distance of ~12 cm from the source (Figure 2A). The 3:1 Ar/O₂ mixture is leaked into the chamber through a needle valve at a pressure of 1×10^{-3} mbar throughout the evaporation. We have shown in previous work that TiO₂ caps form when titanium is evaporated in a 3:1 Ar/O₂ atmosphere of 5×10^{-3} mbar.⁴⁰ Each deposition is recorded on video in order to track the deposition rate. The deposition rate is varied by adjusting the current applied to the tungsten filament. Average deposition rates range from 0.08 to 1.5 nm/s for experiments reported here. The iron pellet is completely melted with the shutter closed before the deposition starts in order to ensure a uniform deposition. 17, 34, and 50 nm (as measured by crystal balance) of iron oxide are deposited at various average deposition rates in a line-of-sight geometry resulting in Janus particles with 50% surface coverage. The three glass slides are sonicated for 10 min in 40 mL of deionized water dispersing the particles evenly in the solution. The dispersion is split into two portions of 20 mL. One portion is used to assemble the particles under a magnetic field immediately after the sonication. The second portion is stored in the refrigerator overnight allowing the Janus particles to settle. Then, 15 mL of the supernatant is removed to increase the particle concentration for assembly at a 4 times higher volume fraction. In addition, the resistivity of a continuous section (2.34 cm) of the iron oxide deposit, remaining on the glass slide after particle removal, is measured with a two-point probe Keithley multimeter for every sample. Resistance values for samples with similar assembly behavior are then reported as an average resistance with one standard deviation.

Figures 2B and 2C show a schematic top and side view of the experimental setup used for magnetic field assembly, respectively. 20 μL of the Janus particle solution is placed into a silicone well adhered to a glass slide and subsequently covered with a microscope cover slide to prevent evaporation. The Janus particles randomly disperse in the cell, and the solution is allowed to equilibrate for ~1 min prior to application of the magnetic field. The 0.08 T U-shaped permanent magnet is placed around the sample to induce a constant external magnetic field. Generally, samples are exposed to the magnetic field for 30 min, and images are collected every 5 min. Structures are imaged

near the bottom surface of the cell in order to reduce the effects of focus variations as structures translate in the z -direction. For some samples, assembly is monitored continuously at 10 frames/s. In selected cases, samples are assembled and dried in a silicone well, mounted onto a silicon wafer, for further characterization by SEM after completion of solvent evaporation (~ 5 h) under continuous magnetic field exposure.

3. RESULTS

In the following section, the behavior observed for iron oxide-capped Janus particles in an applied magnetic field is presented in two parts: (i) the characteristic assembly structure produced, after magnetic field exposure, as a function of deposition rate and cap thickness, and (ii) the chain growth mechanism as a function of assembly time and Janus particle volume fraction.

Figure 3 shows the deposition thickness plotted versus deposition time for 30 iron oxide cap depositions of 50 nm

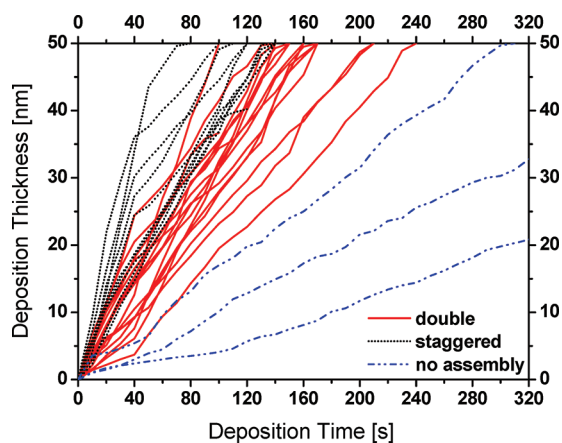


Figure 3. Deposition thickness plotted versus deposition time for iron oxide cap depositions of 50 nm. The various line patterns illustrate the magnetic field assembly behavior observed. Dashed black line: staggered chain structure; solid red line: double chain structure; dash-dotted blue line: no assembly.

thickness. The curves depicted are based on the videos taken during the deposition process (see experiment details) and correlated with the assembly behavior observed. The assembly of these 30 samples is found to be highly dependent on the deposition rate. The deposition rate curves corresponding to different assembly behaviors are distinguished by line type and color. Black (dashed) lines indicate 10 samples that show a staggered chain structure (see Figure 1A) in their assembly, while red (solid) lines depict 17 samples with a double chain structure (see Figure 1B). The blue (dash-dotted) lines are three samples that show no assembly in the magnetic field (see Figure 1C). Fitting of the deposition thickness vs time curves in Figure 3 with linear fits reveals that particles with iron oxide caps deposited at average rates above 0.36 nm/s exhibit a staggered chain structure, between 0.50 and 0.21 nm/s form double chains, and below 0.16 nm/s show no assembly. Note, at certain average deposition rates, i.e., between 0.36 and 0.50 nm/s as well as 0.16 and 0.21 nm/s, two assembly behaviors may be observed simultaneously. These regions are referred to as structural transition regions.

To determine if the cap thickness influences assembly behavior, Janus particles are created with three distinct cap thicknesses at fixed deposition rates. Figure 4 displays the deposition thickness vs time curves obtained for iron oxide

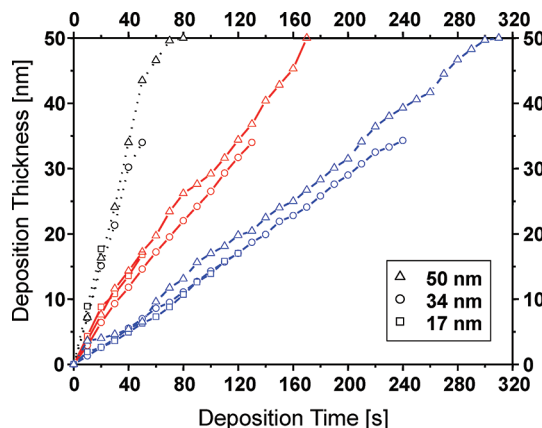


Figure 4. Comparison of assembly behavior results for 17, 34, and 50 nm thick depositions. Iron oxide cap deposition thickness is plotted versus deposition time. Dashed black line: staggered chain structure; solid red line: double chain structure; dash-dotted blue line: no assembly. Open triangle: 50 nm; open circle 34 nm; open square: 17 nm.

depositions at three average deposition rates of 0.76 ± 0.08 , 0.30 ± 0.04 , and 0.15 ± 0.01 nm/s and the resulting assembly behavior for Janus particles with oxide cap thicknesses of 17, 34, and 50 nm (crystal balance). The black (dashed), red (solid), and blue (dash-dotted) lines indicate samples forming staggered chains, double chains, and no assembly, respectively. Triangles, circles, and squares indicate 50, 34, and 17 nm cap thickness, respectively. Additional analysis of the iron oxide residue left behind on the glass slide (after particle removal) with AFM reveals that the crystal balance accurately monitors the iron oxide deposition despite the variation in deposition rate. AFM measurements for samples with 17 nm depositions yield thicknesses of 17.1 ± 0.4 , 17.0 ± 0.5 , and 17.3 ± 0.6 nm for staggered, double, and no assembly samples, respectively. The 34 nm deposition samples are measured to be 34.1 ± 1.1 , 34.1 ± 1.1 , and 34.2 ± 1.0 nm thick for staggered, double, and no assembly samples, respectively. For 50 nm depositions, film thicknesses of 49.0 ± 1.3 , 49.3 ± 0.9 , and 49.9 ± 1.0 nm are obtained for staggered, double, and no assembly samples, respectively. However, it must be noted that while the cap thickness does not appear to have an effect on assembly behavior, it does affect the structural stability of the resulting chains (see below). Resistivity measurements for films obtained from iron deposited in vacuum yield 0.10 ± 0.04 k Ω , and those deposited at average deposition rates of 0.76 ± 0.08 , 0.30 ± 0.04 , and 0.15 ± 0.01 nm/s in a 3:1 Ar/O₂ atmosphere result in 0.5 ± 0.2 k Ω (staggered chain), 2.7 ± 0.7 to 110 ± 50 k Ω (double chain), and >5 M Ω (no assembly), respectively.

Figure 5 shows representative SEM images of dried assemblies of 2.4 μ m iron oxide-capped Janus particles displaying staggered chain (Figure 5A), double chain (Figure 5B), and no assembly behavior (Figure 5C). The scale bar in all three images is 5 μ m. Bright areas on the particle surface are iron oxide caps and darker areas are unmodified polystyrene. The difference in contrast is due to higher electron density of iron oxide compared to polystyrene. Note that several of the Janus particles show half-circular defects in their cap rim. This defect is a result of shadow effects occurring during cap deposition due to partial close packing of particles in the loosely packed monolayer. The SEM images of the staggered and double chain structures (Figure 5A,B) show that the iron

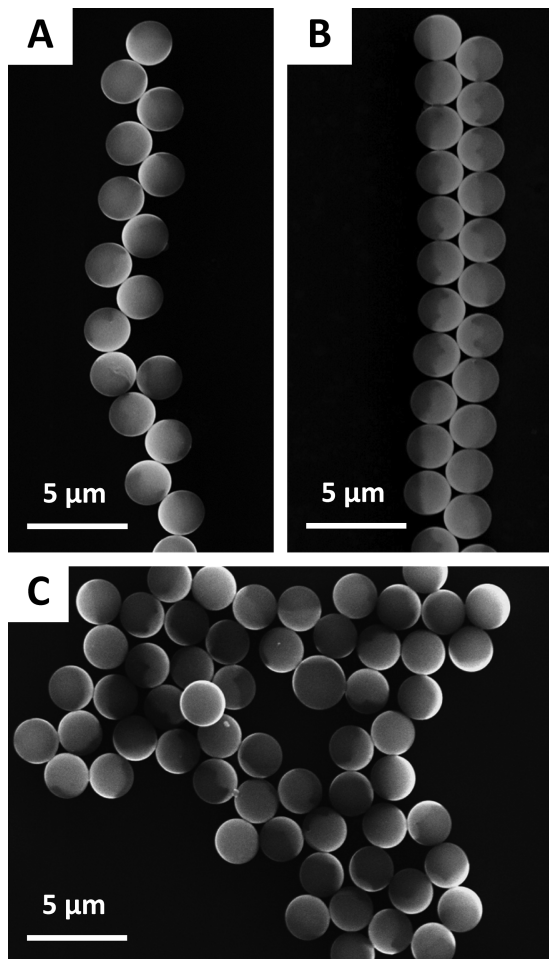


Figure 5. High-resolution scanning electron microscopy images of particle assemblies obtained after complete drying of the solution under continuous exposure to the magnetic field: (A) staggered chain structure, (B) double chain structure, and (C) no assembly. The scale bar in all three images is 5 μm . Lighter areas on the particles are iron oxide caps, and darker areas are unmodified polystyrene particle.

oxide caps touch and are oriented toward the center of the chain, an arrangement that is very similar to that observed for gold-capped Janus particles when assembled in an AC field.²² In contrast to the AC field assembly, magnetic Janus particles stay assembled, due to their magnetization, when dried in the presence of a magnetic field, allowing for identification of particle orientation. However, the convective forces present during drying lead to bending and shearing of the structures resulting in less ordered chain arrangements when compared to the straight chains observed during assembly in solution. This disorder is especially apparent in the staggered chain image (Figure 5A), where caps are connected to each other, but not as aligned as in the double chain sample (Figure 5B). In the samples that show no assembly (Figure 5C), the particle caps are found to be randomly oriented. The particle clustering observed for the “no assembly” particles is caused by capillary and convective forces during drying of the solution.

In addition to the iron oxide deposition rate, other parameters can affect the observed assembly behavior with respect to chain length and number of chains formed. The assembly time, the particle volume fraction of the particle solutions used, and the particle dispersion are the three major factors affecting the final chain length and the number of chains

formed. Unsurprisingly, a higher particle volume fraction leads to longer chains formed in the same time period. Less uniformly dispersed particle solutions, i.e., containing areas with disproportionately high particle concentrations, tend to form longer, but fewer, chains. The chain growth mechanism observed can be described as follows.

Without an applied magnetic field, the iron oxide Janus particles are randomly oriented, show typical Brownian motion, and exist mainly as individual particles with a few doublets or triplets (<5%). After the magnetic field is added, the iron oxide Janus particles are magnetized, and particles within a radius of ~10 μm interact with each other and assemble into preoriented doublets with angles of $\alpha_{DC} = 52 \pm 3^\circ$ and $\alpha_{SC} = 43 \pm 7^\circ$ for double and staggered chains, respectively. Within these particle doublets, the iron oxide hemispheres are facing each other and point in alternating directions along the length of the chain. Particle doublets and triplets observed prior to the application of the magnetic field result from the adhesion of the polystyrene particles in the initial monolayer. The iron oxide caps in such structures are fixed in a single direction causing them to manifest as discontinuities or termination points in the subsequently assembled structures. Careful analysis of the videos obtained from optical microscopy shows that particles sample each other by rotating and sliding along the particle surface in an attempt to locate the lowest energy position (Supporting Information, videos V1–V3). As the assembly process continues, the preoriented doublets connect with other single particles and/or doublets resulting in the formation of short chains (≤ 5 particles). Subsequently, the short chains and the remaining doublets and single particles further interact with each other to form longer chains (≥ 5 particles). Chains with more than 5 particles are found to settle due to their increased weight. As a result, single particles and shorter chains move toward the settled chains. Once near a settled chain, they move along the chain length toward the terminus. Once there, the particle connects by reorienting itself to fit the overall chain structure. As particles assemble into longer chain structures, the distance between chains and particles exceeds the interaction range of ~10 μm and chain formation ceases. When the solution is allowed to dry completely, the long chains move toward each other, resulting in two-dimensional bundles of chains. The specific self-assembly process for both double (video V2) and staggered (video V1) chain structures is similar, but not identical due to the higher assembly speed (1.5 times on average) of the particle doublets in a double chain sample when compared to that of a staggered chain sample.

Figure 6 summarizes optical microscope images of iron oxide-capped Janus particle assemblies after 25 min of assembly for particles with cap thicknesses of 17, 34, and 50 nm (from top to bottom) obtained at deposition rates varying from 1 to 0.25 to 0.1 nm/s (left to right). A closer inspection of images as those shown in Figure 6A,B allows for the determination of a particle–particle center distance, d , and particle angle, Θ , within the chain. In the staggered samples, the distance between particle centers on one side of the chain is $d_{SC} = 2.95 \pm 0.09 \mu\text{m}$. The angle formed by two particles from one side with a corresponding third particle on the other side of the chain is $\Theta_{SC}' = 80 \pm 10^\circ$ with a doublet orientation of $\alpha_{SC}' = 50 \pm 5^\circ$ slightly larger than the angle measured for the preoriented doublets, $\alpha_{SC} = 43 \pm 7^\circ$. In the double chain sample the adjacent particles are connected to each other with the average particle–particle distance at $d_{DC} = 2.45 \pm 0.05 \mu\text{m}$, a value close to the mean particle diameter ($2.4 \pm 0.1 \mu\text{m}$), and an

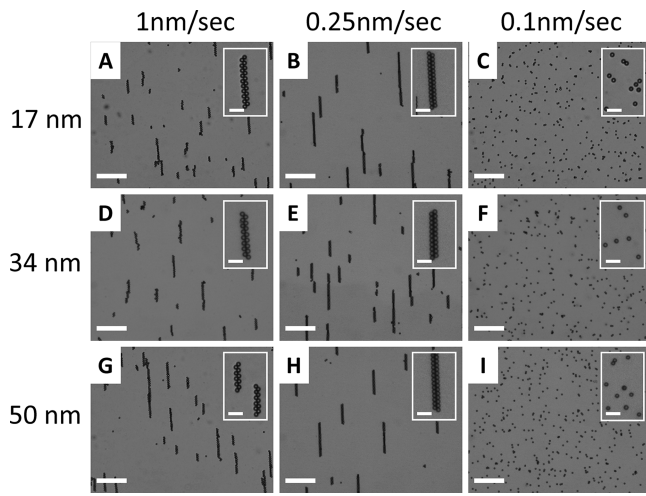


Figure 6. Optical microscope images showing assembled iron oxide-capped Janus particle with cap thicknesses of 17, 34, and 50 nm (from top to bottom) obtained at deposition rates varying from 1 to 0.25 to 0.1 nm/s (left to right) within 25 min. The scale bars in all images and insets are 50 and 10 μm , respectively.

angle of $\Theta_{\text{DC}}' = 62 \pm 10^\circ$ with a doublet orientation in the chain of $\alpha_{\text{DC}}' = 59 \pm 5^\circ$.

Another important property of the chain structures is their stability during the final drying step, when capillary and convective forces affecting the chains are maximized. The double chains made from particles with 50 and 34 nm caps retain their structure during drying without fragmentation, while those with 17 nm caps fall apart during drying. Staggered chains are found to break into smaller chain fragments for each of the three cap thicknesses due to the shearing and the bending induced during the drying indicating that their magnetic interaction may be weaker.

4. DISCUSSION

The three assembly configurations observed for the iron oxide Janus particles suggest a variation in the physical properties of the iron oxide caps. In the following, we identify the specific type of iron oxide as the primary cause behind these variations and show that the assembly behavior is controlled by systematically varying the rate with which iron is evaporated in a 3:1 Ar/O₂ atmosphere at 1×10^{-3} mbar. For iron oxide Janus particles with a cap thickness of less than or equal to 50 nm, the exposure to a magnetic field produces staggered chain, double chain, or no assembly behavior at average deposition rates of 1, 0.25, or 0.1 nm/s, respectively. The marked difference between the three assembly behaviors suggests that a unique variation of iron oxide is responsible for each final configuration. This statement is further supported by the fact that each individual sample, created outside of the structural transition regions, exhibits only one type of assembly behavior.

In order to determine the degree of oxidation of iron atoms traveling from the source to the particle surface, we utilize mean free path calculations.⁴¹ The 3:1 Ar/O₂ mixture is leaked into the evaporator at a pressure of 1×10^{-3} mbar. The distance between the iron source and the sample stage inside the evaporator chamber is ~ 12 cm. Equation 1 can be used to calculate the mean free path for a single gas system, d_0 is the molecular diameter, n is the gas density.

$$\lambda = \frac{1}{\sqrt{2} \pi d_0^2 n} \quad (1)$$

According to eq 1, the mean free path of pure molecular oxygen is 9.13 cm using $d_0 = 3.2 \times 10^{-10}$ m. However, the system also contains iron atoms, which are assumed to be in a gaseous state. This fact requires the modification of eq 1 into the following form, eq 2:⁴¹

$$\lambda_a = \left[\sqrt{2} \pi n_a d_a^2 + \left(1 + \frac{v_b^2}{v_a^2} \right)^{1/2} n_b \frac{\pi}{4} (d_a + d_b)^2 \right]^{-1} \quad (2)$$

$$v = \left(\frac{8kT}{\pi m} \right)^{1/2} \quad (3)$$

where v_a and v_b are the average particle velocities calculated according to eq 3. From eq 2, we calculate the mean free path of an iron atom in an iron/oxygen mixture to be $\lambda_{\text{Fe}} = 9.92$ cm. The mean free path of $\lambda_{\text{Fe}} = 9.92$ cm compared to the source-sample distance of ~ 12 cm indicates that one iron atom can only collide with one oxygen molecule before it reaches the PS particle surface. Additionally, from a statistical point of view, only every fourth iron atom will interact with an oxygen molecule since a 3:1 Ar/O₂ mixture is used. On the basis of this calculation, we can assume that we deposit bare iron atoms onto the PS particle surface. Note that the reaction of room temperature iron atoms with O₂ has been reported to be endothermic by 21 kcal/mol⁴² with an upper second-order rate constant limit of $k < 1 \times 10^{-4}$ cm³ molecule⁻¹ s⁻¹ for reaction in a 5:2 Ar/O₂ atmosphere.⁴³ However, iron has also been shown to rapidly oxidize at higher temperatures.^{42,45} Since the iron atoms undergo only one collision with the background gas, it is very likely that they have residual kinetic energy when they reach the PS particle surface, enabling their subsequent reaction with oxygen molecules impinging on the particle surface. The degree of oxidation of each successive iron layer is thus directly dependent on the rate of evaporation of iron.

$$\Gamma = nv/4 \quad (4)$$

Equation 4 gives the particle flux of an ideal gas striking a unit surface. Using eq 4, the number of oxygen molecules that reach the PS particle surface per second can be determined. According to eq 4, the particle flux for molecular oxygen is $\Gamma = 6.05 \times 10^9$ O₂ molecules per particle cap per second. Γ is fixed for all depositions because the pressure of the 3:1 Ar/O₂ mixture is constant during deposition.

The number of iron atoms deposited per second on the surface of a single particle is calculated using the average deposition rates and the assumption of uniform cap thickness. For staggered chains, with an average deposition rate of 0.76 nm/s, 3.89×10^8 iron atoms are deposited on a single PS particle per second. For double chains with an average deposition rate of 0.3 nm/s, the number of iron atoms deposited is 1.53×10^8 atoms/s per particle. Finally, for the no assembly system, with an average deposition rate of 0.15 nm/s, the number of iron atoms deposited is 7.67×10^7 atoms/s per particle. From the particle flux of oxygen and the number of iron atoms deposited onto the PS particle surface, we can calculate the ratio of iron to oxygen that reaches a single PS particle per second. For a staggered chain sample the Fe:O₂

ratio is 1:16, for double chain samples the Fe:O₂ ratio is 1:39, and for no assembly samples the Fe:O₂ ratio is 1:79. As a result of these Fe:O₂ ratios, we have access to three oxidation states of iron oxide.

On the basis of the oxidation model of iron discussed above and specific physical properties of each individual Janus particle assembly, we propose a relationship between the average deposition rate and the type of iron oxide produced. Particles carrying an iron oxide cap produced at 1 nm/s assemble into staggered chains. These structures show low resistance to external deformation. Further, the particle caps gradually oxidize and show double chain type assembly when left in water over a period of time (several days to months). This observation suggests that the iron oxide produced at this average deposition rate is nonstoichiometric Fe_{1-x}O, a weakly ferromagnetic compound when produced in thin films (<300 nm).³⁰ The weak ferromagnetism is the result of clusters of defects with an oxygen environment close to that of Fe₃O₄.³³ Note that stoichiometric FeO in bulk is an antiferromagnetic material, which would not show any assembly in a magnetic field. Additionally, the material produced at the 1 nm/s rate has a resistance of 0.5 ± 0.2 kΩ, which is 5 times higher than that of iron deposited in vacuum (0.10 ± 0.04 kΩ) and exhibits a dark gray color in good agreement with the black color of Fe_{1-x}O.³⁸ As we decrease the average deposition rate to 0.25 nm/s the assembly behavior shifts to a more durable double chain structure. This rigidity, coupled with the observed shift to inert behavior when left in an aqueous environment for lengthy periods of time, implies this type of oxide to be Fe₃O₄. Fe₃O₄ is a ferrimagnetic compound, which, when coupled with the effect of the thickness of the iron oxide cap (see above), explains the resilience of the double chain structures when compared with the staggered chain system.³⁰ Furthermore, the resistivity measurements indicate a range of resistances from as low as 2.7 ± 0.7 kΩ to as high as 110 ± 50 kΩ. The low resistance films tend to be dark gray, in agreement with the reported black color of Fe₃O₄ crystals,³⁸ while high resistance films are gray with a yellow tint hinting at a higher degree of oxidation. By this progression the inert material produced at 0.1 nm/s is likely α-Fe₂O₃, which is an antiferromagnetic compound.³⁰ The deposited film shows the highest resistance with values well above 4 MΩ, in good agreement with the reported order of magnitude difference in resistance between Fe₃O₄ and Fe₂O₃.³⁶ The samples also display a reddish-orange color, a property shared by the red-brown α-Fe₂O₃ crystals.³⁸ The antiferromagnetic property explains the nonassembly of this type of Janus particles in the 0.08 T magnetic field used. This type of cap does not change properties after prolonged exposure to air or water, represents the highest oxidation state, and is thus considered the most stable oxidation state.

The preferential assembly into staggered or double chains at constant magnetic field is attributed to the variation in saturation magnetization, M_s , of the respective cap materials. As the chain assembles, the particle position within the chain is determined by the orientation of the initially preoriented doublets. Figure 7 shows schematics of doublets leading to (A) staggered and (B) double chains. According to general dipole interaction rules, two magnetic dipoles have the strongest attractive interaction when they are aligned with each other in the field direction at $\alpha = 0^\circ$, whereas their interaction is most repulsive at $\alpha = 90^\circ$. At angles in between those two extremes, the interaction gradually changes from attractive to repulsive. A single Janus particle approaching the doublet in Figure 7A can

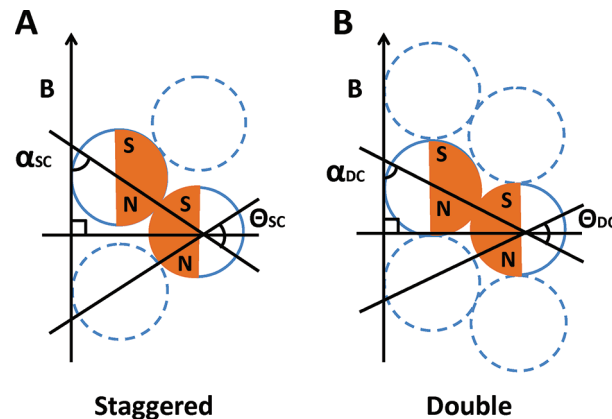


Figure 7. Schematics of preoriented doublets formed upon application of the external magnetic field B leading to (A) staggered chain with $\alpha_{SC} = 43^\circ$ and $\Theta_{SC} = 94^\circ$ and (B) double chain with $\alpha_{DC} = 52^\circ$ and $\Theta_{DC} = 76^\circ$. Shaded (orange) region indicates Fe_xO_y coating. N and S indicate north and south pole, respectively. The angle α describes the orientation of the doublet axis with respect to the magnetic field, and Θ corresponds to the angle between three adjacent particles in a chain.

connect to it in two places indicated by the dashed circles, while a single Janus particle approaching the doublet leading to double chains has four potential binding sites (Figure 7B). The placement of the two binding sites in the staggered chain assembly can be rationalized by the magnetic moment of the incoming particle aligning itself with the magnetic dipole of the existing doublet. In contrast, the doublet leading to double chains (Figure 7B) allows the most attractive alignment of the magnetic moment of the incoming particle with the magnetic moment of one of the two particles in the doublet. The interactions in Figure 7A result in a less packed staggered structure, which is more easily deformed in solution and may be ripped apart during solvent evaporation. In addition, the SEM images shown in Figure 5 indicate that particles in the double chains are more or less locked in their positions within the chain; however, the particles in the staggered chain are capable of rotation within the chain. Since the magnetic field is held constant at 0.08 T in all assembly experiments, the saturation magnetization of the cap material must depend on the deposition rate in order to rationalize the varying assembly behavior observed in a constant magnetic field. The fact that double chains are interacting more strongly compared to staggered chains indicates that the cap material of the staggered chains has a smaller saturation magnetization than that of the double chains, in good agreement with the room temperature literature values of $(M_s(\text{Fe}_{1-x}\text{O})) = 65\text{--}198 \text{ emu/cm}^3$,^{33,34} $M_s(\text{Fe}_3\text{O}_4) = 254\text{--}480 \text{ emu/cm}^3$,^{34,46} and $M_s(\alpha\text{-Fe}_2\text{O}_3) = 3 \text{ emu/cm}^3$.^{33,46}

More specifically, Kim et al.³⁴ studied the dependence of iron oxide film composition as a function of oxygen flow rate and film thickness for films deposited with reactive RF magnetron sputtering using an Fe target. They found single phases of pure Fe, Fe_{1-x}O, Fe₃O₄, and α-Fe₂O₃ with increasing O₂ flow rate (0–2.2 sccm) for iron oxide films deposited on room temperature substrates with thicknesses below 75 nm. The stability of the phases is attributed to a large in-plane compressive stress. In our study the films are ≤50 nm and rather than varying the oxygen flow rate, we vary the iron deposition rate in a constant 3:1 Ar/O₂ atmosphere. As a result, the number of oxygen molecules impinging on the cap surface per evaporated nanometer of cap material increases by a factor

of 2 each time as the deposition rate decreases leading to more oxidized caps.

As discussed in the Introduction, Smoukov et al.⁸ reported the formation of double chains from 8 nm iron-capped particles and staggered chains with 34 nm iron-capped particles. Further, tapping of the experimental cell after removal of the magnetic field resulted in breakup of the double chain configuration, whereas the staggered chain configuration stayed intact. These results imply that the staggered chain configuration is the stronger one of the two, in disagreement with the observations made for the iron oxide-capped particles reported here. The two observations can be reconciled when postdeposition oxidation of the iron caps is taken into account. EDS data obtained from SEM measurements using an EDAX detector (Supporting Information, Figure S1) show that particles capped under high-vacuum conditions ($\sim 10^{-6}$ mbar) with iron (50 ± 3 nm) already contain oxygen (Fe:O ratio = 1:0.17) after transport from the PVD chamber to the SEM, in good agreement with room temperature oxidation of polycrystalline iron^{47,48} and are further oxidized when exposed to an aqueous environment (Fe:O = 1:1.81 after a 48 h exposure to water).⁴⁹ Taking this oxidation behavior into account, it is likely that the 8 nm cap used in Smoukov et al.'s⁸ experiments is fully oxidized, while the 34 nm cap is an iron cap covered with an iron oxide shell. As a result, the 8 nm capped particles would be expected to show double chain behavior and 34 nm capped particles should show staggered chain behavior, due to the strong magnetic properties of the iron core ($M_s(\text{Fe}) = 1745$ emu/cm³).⁵⁰ The differences in relative strengths observed for double and staggered assemblies can also be explained by the extent of oxidation of the iron caps. The soft ferromagnetic iron core in the 34 nm capped particles provides inherent stability to the staggered arrangement when compared to the iron oxide-capped particles in our study ($M_s(\text{Fe}) = 1745$ emu/cm³ vs $M_s(\text{Fe}_{1-x}\text{O}) = 65\text{--}198$ emu/cm³).^{33,34,50} Additionally, the weakness of the double chain arrangements composed of the 8 nm capped particles can be attributed to oxidation and the small amount of material in the cap. For example, our 50 nm capped iron oxide particles with double chain behavior have 6 times thicker caps. This argument is further supported by our observation of reduced stability correlated with decreasing cap thickness; i.e., double chains assembled from particles with 17 nm caps do not survive the drying process (see above).

Figure 8 shows the generalized average deposition rate diagram for the Fe_xO_y system with two structural transition regions. If the deposition rate is higher than 0.5 nm/s or done in the absence of the 3:1 Ar/O₂ mixture, the assembly only yields staggered chains. A deposition rate between 0.33 and 0.50 nm/s, i.e., structural transition region I, leads to samples with double, staggered, or mixed chains. Holding the deposition rate between 0.22 and 0.33 nm/s during the evaporation leads to samples with pure double chain structures. If the deposition rate is between 0.17 and 0.22 nm/s, i.e., the structural transition region II, the resulting particles would assemble into double chains or show no assembly. If the deposition rate is lower than 0.17 nm/s, no chains assemble. Figure 8 is valid for cap thicknesses from 17 to 50 nm and highlights the fact that the average deposition rate of iron in a 3:1 Ar/O₂ atmosphere of 1×10^{-3} mbar is the key parameter for controlling the assembly behavior of iron oxide Janus particles. Further studies will investigate iron oxide caps with protective layers, which may lead to particles with Fe_{1-x}O compositions that are stable in aqueous environments over longer periods of times.

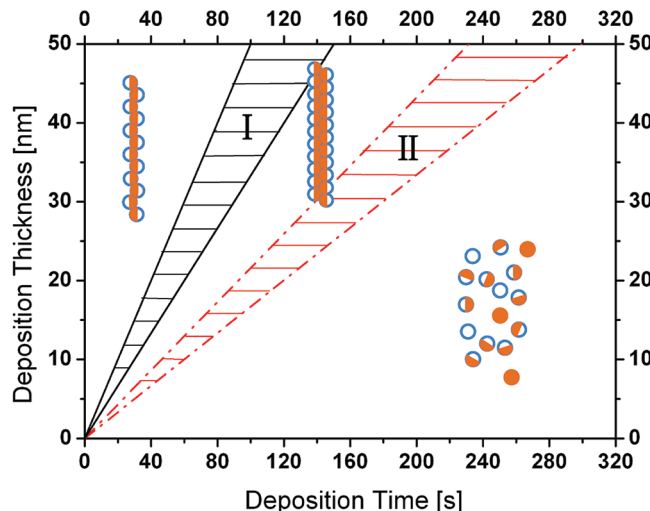


Figure 8. Generalized assembly behavior chart as a function of deposition thickness and deposition time indicating regions of pure staggered chain, double chain, and no assembly behavior. Shaded areas indicate transition regions, where deposition parameters lead to samples that show either of the two adjacent assembly behaviors.

5. CONCLUSION

We have shown that varying the deposition rate of iron in an oxidizing atmosphere leads to iron oxide-capped Janus particles with varying degrees of oxidation resulting in distinct assembly behaviors. Three types of behavior, i.e., (i) staggered chains for Fe_{1-x}O caps, (ii) double chains for Fe_3O_4 caps, and (iii) no assembly for $\alpha\text{-Fe}_2\text{O}_3$, are observed after exposure of the iron oxide-capped Janus particles to an external magnetic field (0.08 T) for a period of time. Samples obtained at a specific average deposition rate with varying cap thickness show the same assembly behavior. Mean free path analysis reveals that the iron is oxidized once it is deposited on the particle surface due to impinging O₂ molecules. Further, chain structure and stability are correlated to preorientation of the initially formed doublets and saturation magnetization of the various iron oxides, respectively.

■ ASSOCIATED CONTENT

Supporting Information

Three videos of the assembly process for iron oxide-capped Janus particles showing staggered (V1), double (V2), and no assembly behavior (V3). This material is available free of charge via the Internet at <http://pubs.acs.org>.

■ AUTHOR INFORMATION

Corresponding Author

*E-mail: kretzschmar@ccny.cuny.edu.

■ ACKNOWLEDGMENTS

This project is supported by the National Science Foundation under Award NSF-CBET 0644789. Alexander Richter is acknowledged for helpful assistance at the initial stages of this project. A.R. acknowledges a stipend from the NSF PREM sponsored Undergraduate Research Fellow Program DMR#-0934206.

■ REFERENCES

- (1) Kretzschmar, I.; Song, J. H. K. *Curr. Opin. Colloid Interface Sci.* 2011, 16, 84.

- (2) Dyab, A. K. F.; Ozmen, M.; Ersozb, M.; Paunov, V. N. *J. Mater. Chem.* **2009**, *19*, 3475.
- (3) Yuet, K. P.; Hwang, D. K.; Haghgoie, R.; Doyle, P. S. *Langmuir* **2009**, *26*, 4281.
- (4) Tartaj, P. *Curr. Nanosci.* **2006**, *2*, 43.
- (5) Ghosh, A.; Sheridan, N. K.; Fischer, P. *Small* **2008**, *4*, 1956.
- (6) Erb, R. M.; Jenness, N. J.; Clark, R. L.; Yellen, B. B. *Adv. Mater.* **2009**, *21*, 4825.
- (7) Anker, J. N.; Koppelman, R. *Appl. Phys. Lett.* **2003**, *82*, 1102.
- (8) Smoukov, S. K.; Gangwal, S.; Marquez, M.; Velev, O. D. *Soft Matter* **2009**, *5*, 1285.
- (9) Behrend, C. J.; Anker, J. N.; Koppelman, R. *Appl. Phys. Lett.* **2004**, *84*, 154.
- (10) Takei, H.; Shimizu, N. *Langmuir* **1997**, *13*, 1865.
- (11) Cameron, L.; Footer, M.; van Oudenaarden, A.; Theriot, J. *Proc. Natl. Acad. Sci. U. S. A.* **1999**, *96*, 4908.
- (12) Link, J. R.; Sailor, M. J. *Proc. Natl. Acad. Sci. U. S. A.* **2003**, *100*, 10607.
- (13) Crowley, J. M.; K. Sheridan, N.; Romano, L. *J. Electrostat.* **2002**, *55*, 247.
- (14) Nisisako, T.; Torii, T.; Takahashi, T.; Takizawa, Y. *Adv. Mater.* **2006**, *18*, 1152.
- (15) Sheridan, N. In *Flexible Flat Panel Displays*; Crawford, G., Ed.; John Wiley and Sons: New York, 2005; Vol. 20, p 393.
- (16) Liu, Y. D.; Kim, J. E.; Choi, H. J. *Macromol. Rapid Commun.* **2011**, *32*, 881.
- (17) Fang, F. F.; Liu, Y. D.; Choi, H. J.; Seo, Y. *ACS Appl. Mater. Interfaces* **2011**, *3*, 3487.
- (18) McNaughton, B. H.; Agayan, R. R.; Wang, J. X.; Koppelman, R. *Sens. Actuators, B* **2007**, *121*, 330.
- (19) Chen, C.-H.; Abate, A. R.; Lee, D.; Terentjev, E. M.; Weitz, D. A. *Adv. Mater.* **2009**, *21*, 3201.
- (20) Paunov, V. N.; Cayre, O. J. *Adv. Mater.* **2004**, *16*, 788.
- (21) Suzuki, D.; Kawaguchi, H. *Colloid Polym. Sci.* **2006**, *284*, 1471.
- (22) Gangwal, S.; Cayre, O. J.; Velev, O. D. *Langmuir* **2008**, *24*, 13312.
- (23) Gangwal, S.; Cayre, O. J.; Bazant, M. Z.; Velev, O. D. *Phys. Rev. Lett.* **2008**, *100*, 058302.
- (24) Kim, S.-H.; Sim, J. Y.; Lim, J.-M.; Yang, S.-M. *Angew. Chem., Int. Ed.* **2010**, *49*, 3786.
- (25) Gangwal, S.; Pawar, A. B.; Kretzschmar, I.; Velev, O. D. *Soft Matter* **2010**, *6*, 1413.
- (26) Kavich, D. W.; Hasan, S. A.; Mahajan, S. V.; Park, J.-H.; Dickerson, J. H. *Nanoscale Res. Lett.* **2010**, *5*, 1540.
- (27) Caricato, A. P.; Gorbachuk, N. T.; Korduban, A. M.; Leggieri, G.; Luches, A.; Mengucci, P.; Mulenko, S. A.; Valerini, D. *J. Vacuum Sci. Technol., B* **2010**, *28*, 295.
- (28) Park, B. J.; Fang, F. F.; Choi, H. J. *Soft Matter* **2010**, *6*, 5246.
- (29) Mi, W. B.; Liu, H.; Li, Z. Q.; Wu, P.; Jiang, E. Y.; Bai, H. L. *J. Phys. D: Appl. Phys.* **2006**, *39*, 5109.
- (30) Kim, K. J.; Moon, D. W.; Lee, S. K.; Jung, K.-H. *Thin Solid Films* **2000**, *360*, 118.
- (31) Greenwood, N. N.; Howe, A. T. *J. Chem. Soc., Dalton Trans.* **1972**, 116.
- (32) Dimitrov, D. V.; Hadjipanayis, G. C.; Papaefthymiou, V.; Simopoulos, A. *IEEE Trans. Magn.* **1997**, *33*, 4363.
- (33) Dimitrov, D. V.; Hadjipanayis, G. C.; Papaefthymiou, V.; Simopoulos, A. *J. Vacuum Sci. Technol., A* **1997**, *15*, 1473.
- (34) Kim, Y. K.; Oliveria, M. *J. Appl. Phys.* **1994**, *75*, 431.
- (35) Pan, L.; Zhang, G.; Fan, C.; Qiu, H.; Wu, P.; Wang, F.; Zhang, Y. *Thin Solid Films* **2005**, *473*, 63.
- (36) Mei, Y.; Zhou, Z.-J.; Luo, H. L. *J. Appl. Phys.* **1987**, *61*, 4388.
- (37) Aronniemi, M.; Lahtinen, J.; Hautojärvi, P. *Surf. Interface Anal.* **2004**, *36*, 1004.
- (38) *Handbook of Chemistry and Physics*, 79th ed.; CRC Press: Boca Raton, FL, 1998.
- (39) Prevo, B. G.; Velev, O. D. *Langmuir* **2004**, *20*, 2099.
- (40) Song, J. H.; Kretzschmar, I. *ACS Appl. Mater. Interfaces* **2009**, *1*, 1747.
- (41) O'Hanlon, J. F. *A User's Guide to Vacuum Technology*, 3rd ed.; John Wiley & Sons, Inc.: Hoboken, NJ, 2003.
- (42) Chertihin, G. V.; Saffel, W.; Yustein, J. T.; Andrews, L.; Neurock, M.; Ricca, A.; Bauschlicher, C. W. *J. Phys. Chem.* **1996**, *100*, 5261.
- (43) Mitchell, S. A.; Hackett, P. A. *J. Chem. Phys.* **1990**, *93*, 7822.
- (44) Davies, M. H.; Simnad, M. T.; Birchenall, C. E. *J. Met.* **1951**, *3*, 889.
- (45) Slattery, J. C.; Peng, K.-Y.; Gadalla, A. M.; Gadalla, N. *Ind. Eng. Chem. Res.* **1995**, *34*, 3405.
- (46) Pullaiah, G.; Irving, E.; Buchan, K. L.; Dunlop, D. *J. Earth Planet. Sci. Lett.* **1975**, *28*, 133.
- (47) Graat, P. C. J.; Somers, M. A. J.; Vredenberg, A. M.; Mittemeijer, E. J. *J. Appl. Phys.* **1997**, *82*, 1416.
- (48) Roosendaal, S. J.; Vredenberg, A. M.; Habraken, F. H. P. M. *Phys. Rev. Lett.* **2000**, *84*, 3366.
- (49) Song, J. H. PhD Thesis, City College of New York, 2009.
- (50) Gengnagel, H.; Arrott, A. *J. Appl. Phys.* **1968**, *39*, 669.